Article

Effect of Protein Loading Density on the Structure and Biopreservation Efficacy of Metal-Organic Frameworks

Yixuan Wang [1,2], Sirimuvva Tadepalli [3,†], Harsh Baldi [1,2], Jeremiah J. Morrissey [1,4], and Srikanth Singamaneni [1,2,4,*]

[1] Department of Mechanical Engineering and Materials Science, Washington University in St. Louis, St. Louis, MO 63130, USA
[2] Institute of Materials Science and Engineering, Washington University in St. Louis, St. Louis, MO 63130, USA
[3] Radiation Oncology-Radiation Physics, Stanford School of Medicine, Stanford, CA 94305, USA
[4] Siteman Cancer Center, Barnes-Jewish Hospital, and Washington University School of Medicine in St. Louis, St. Louis, MO 63130, USA
* Correspondence: singamaneni@wustl.edu
† Present Affiliation: Department of Immunology, School of Medicine, Stanford University, Stanford, CA 94305, USA
Received: 9 September 2024; Revised: 31 October 2024; Accepted: 5 November 2024; Published: 20 November 2024

Abstract: Metal-organic frameworks (MOFs) have emerged as attractive bioencapsulants for preserving the structure and function of various biomolecules against harsh environmental conditions. However, the effect of the loading density of the biomolecules on the structure, physical properties, and biopreservation efficacy of MOF crystals remains elusive. We investigated the structure and properties of zeolitic imidazolate framework (ZIF)-90 crystals as a function of the loading density of a model protein, bovine/human serum albumin (BSA/HSA). We show that the total protein concentration in the MOF growth reaction solution significantly affects the morphology, degree of crystallinity, and biopreservation efficacy of the MOF crystals. The structure integrity and immunologic functionality of albumin remained well-preserved within an optimal protein concentration range of 0.1–1 mg/mL. The proposed optimal range of biomolecule concentration during in situ MOF growth is critical for guiding future research and design endeavors within the rapidly evolving field of MOF-biomedical applications, offering exciting possibilities for biopreservation, drug delivery, and diagnostics.

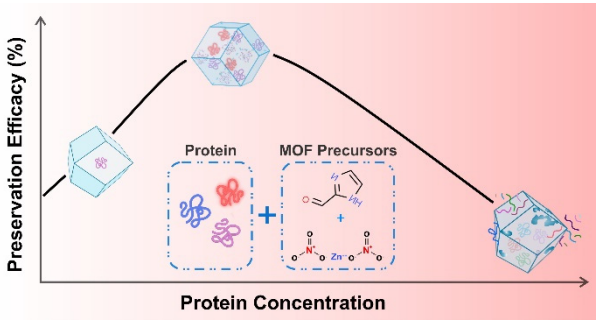

Keywords: metal-organic framework; biopreservation; protein loading density; MOF biocomposites

1. Introduction

The stability and functionality of biomolecules in various biofluids and biospecimens are critical considerations in biomedical research and clinical diagnosis [1–3]. The accuracy of diagnostic information obtained from analyzing biofluids heavily depends on the stability and functionality of the biomolecules [2]. Unfortunately, many molecular biomarkers, particularly proteins, are prone to losing their structure and biofunctionality due to poor stability under ambient and elevated temperatures [4,5]. To accurately measure biomolecules in clinical labs, an extensive 'cold chain' distribution network is required [6], which is often impractical and unaffordable in resource-limited settings, especially given the existential threat of climate change. To address this challenge, extensive efforts have been dedicated to developing refrigeration-free techniques for preserving biospecimens and other biological entities [6–12].

Metal-organic frameworks (MOF) are crystalline [13,14], nanoporous materials comprised of metal clusters and bridged by organic ligands. A subclass of MOFs, zeolitic imidazolate frameworks (ZIFs), are comprised of metal nodes and imidazolate linkers held together by metal-coordination bonds. Over the past decade, ZIFs have emerged as highly promising encapsulants for a diverse range of biomolecules, including DNA [8], peptides [15],

therapeutic proteins [16,17], enzymes [15,18,19], vaccines [20–22], living cells [23], and immobilized antibodies in biodiagnostic devices [24]. ZIFs are particularly attractive as encapsulants and preservatives due to their remarkable properties, which include high thermal and chemical stability, tunable pore size, high loading capacity, biocompatibility, and mild synthesis conditions and on-demand dissociation. ZIF crystals can be formed under mild aqueous conditions (i.e., at room temperature and physiological pH), readily encapsulating biomolecules and effectively preserving their structural and functional integrity against denaturation and degradation under harsh conditions.

Encapsulation of various biological entities within MOFs has been achieved through two primary pathways: molecular infiltration and biomineralization [11,25]. Molecular diffusion involves the passive transport of biomolecules into pre-synthesized MOFs [26], but this method is limited by the stringent requirements of guest size and surface chemistry of MOFs, potentially denaturing biomolecules during the formation of MOF-protein inclusion complexes. ZIF-90 possesses a aperture size of approximately 0.35 nm [14], which is significantly smaller than the dimensions of most proteins. As a result, the encapsulation and preservation of proteins within ZIF-90 using diffusion-based methods are inherently challenging. The limited pore size restricts the diffusion of larger biomolecules into the internal cavities of the ZIF-90 crystals, thereby hindering effective protein loading and storage. The second method involves the in situ growth of MOF crystals in the presence of the biological species [7], offering a unique opportunity to create precisely tailored MOF-biomolecule composites with enhanced stability of the encapsulated biomolecules [10,27–29]. This interest in utilizing MOFs for hosting and delivering biological guest materials has prompted investigations into the interaction between MOFs and biomolecules through experimental and computational methods [25–28,30–40]. However, the structure and properties of MOFs, biomolecules, and their interfaces in MOF-based biocomposites remain elusive: (i) what is the effect of the loading density of the proteins on the structure and properties of MOF crystals? (ii) how does the biopreservation efficacy of MOF crystals vary with the loading density of the proteins? (iii) what are the optimal conditions for protein encapsulation and preservation within MOF crystals?

In this study, we reveal how the total protein concentration in the reaction solution governs the morphology, crystallinity, thermal stability, and preservation efficacy of the in situ-synthesized ZIF-90 crystals. The morphological and structural evolution of protein-encapsulated ZIF-90 crystals were explored with environmental scanning electron microscope (ESEM), transmission electron Microscope (TEM), Brunauer-Emmett-Teller (BET), X-ray diffraction (XRD), and differential scanning calorimetry (DSC). The structure and functionality of protein were evaluated by using a plasmonic-fluor-linked enzyme-linked immunosorbent assay (p-FLISA) and Fourier transform infrared (FTIR) spectroscopy. The crystallinity and thermal stability of MOF crystals progressively decreased with an increase in the protein loading. The biopreservation efficacy of the MOF crystals was maximum at an intermediate protein concentration, determined by the tradeoff between efficient loading/recovery of the protein and optimal encapsulation under harsh environmental conditions.

2. Materials and Methods

2.1. Materials

Human serum albumin (HSA) (H6914), and bovine serum albumin (BSA) (A7030) were purchased from Millipore Sigma (St. Louis, MO, USA), human serum albumin ELISA kits (DY 1455) from R&D Systems (Minneapolis, MN, USA). Plasmonic-fluor–800 was purchased from Auragent Biosciences (St. Louis, MO, USA), while zinc nitrate, 2-imidazolecarboxaldehyde (ICA), ethylenediaminetetraacetic acid (EDTA), polyvinylpyrrolidone (PVP), tween-20, sodium phosphate monobasic, and sodium phosphate dibasic, were purchased from Millipore Sigma (St. Louis, MO, USA). All chemicals were used as received without further purification.

2.2. Methods

2.2.1. Encapsulation of HSA/BSA Proteins with ZIF-90 Crystals

HSA/BSA were diluted 10 times and 30 times with nanopure water. Then each diluted sample was mixed with ICA (320 μL) and 80 μL of zinc nitrate solution, the final concentration of HSA/BSA in each samples are 0, 0.01, 0.05, 0.1, 0.32, 0.5, 0.64, 1, 1.2, 5, 10 and 20 mg/mL. 0.2 wt% PVP were mixed well with ICA before reacting with zinc nitrate solution. The final concentration of ICA was 160 mM and the molar ratio of ICA and zinc nitrate was controlled to be 4:1. After 4 h of incubation at room temperature (20–23 °C), the mixture solution was

centrifuged at 8000 rpm for 15 min. The resultant particles were then rinsed with slightly alkaline nanopure water three times. Finally, the particles were stored at 55 °C for various lengths of time up to 2 weeks.

2.2.2. Protein Recovery

To recover embedded proteins from ZIF-90 crystals, MOF dissociation buffer (0.1 M phosphate buffer with 100 mM EDTA and 0.05% Tween-20 at pH 5.1) was added to each of the tubes and subjected to gentle orbital mixing for 25 min. After protein released from the crystals, the suspension turned from white to clear. To quantify the protein recovery after storage, HSA p-FLISA were performed. The preservation efficacy was calculated by comparing the amount of HSA released from ZIF crystals to the amount of HSA stored at −20° C, a standard cold chain condition, which represents 100%.

2.2.3. Plasmonic-Fluor-Linked Immunosorbent Assay of HSA

Human HSA DuoSet ELISA kit (R&D DY1455) was employed in the study. Specifically, 96-well plates were first incubated with capture antibodies (2 μg/mL in phosphate buffered saline (PBS) overnight at room temperature, followed by blocking with 3% BSA in 1X PBS for 2 h at room temperature. After 3 times washing with PBS containing 0.5% Tween 20 (PBST), 100 μL of serially diluted standard as well as samples (e.g., eluted protein solution) were added into different wells, and the plate was incubated at room temperature for two hours. The plate was washed subsequently and incubated with biotinylated detection antibodies for 2 h, followed by washing and the addition of 100 μL of plasmonic-fluors [3]. Plasmonic-fluors were incubated for 30 min, and the plate was washed three times with PBST. The fluorescence image of the microtiter plate was obtained using a LI-COR CLx fluorescence scanner. The concentration of the protein in unknown samples was determined using standard curve fit with a 4-parameter logistic model.

2.2.4. Statistics

For analyzing the statistical difference between two groups, an unpaired two-tailed t-test with Welch's correction was used. For analyzing the statistical difference between more than two groups, one-way analysis of variance (ANOVA) with a post-hoc Dunnett's significance test was used. Statistical significance of the data was calculated at 95% ($p < 0.05$) confidence intervals. All values are expressed as mean ± s.d.

2.2.5. Material Characterization

X-ray diffraction (XRD) measurements of the samples were performed on a Bruker D8-Advance X-ray powder diffractometer (Madison, WI, USA) using Cu Kα radiation (λ = 1.5406 Å) with scattering angles (2θ) of 5–25°. SEM images were obtained using Thermo Scientific Quattro S Environmental Scanning Electron Microscope (ESEM, Waltham, MA, USA). Transmission electron microscopy images were obtained using a JEOL JEM-2100F field emission instrument (TEM, Akishima, Japan). The surface area was calculated with the Brunauer–Emmett–Teller (BET) equation, and the pore size distribution was calculated by the Barrett–Joyner–Halenda (BJH) method. Attenuated total reflection Fourier transform infrared spectra (ATR-FTIR, Waltham, MA, USA) were obtained using a Nicolet iS10 spectrometer in the range of 400–4000 cm^{-1} at a resolution of 0.48 cm^{-1}, averaging 100 scans. Differential scanning calorimetry (DSC, Greifensee, Switzerland) measurements were performed on a Mettler Toledo STARe DSC1 with a heating rate of 20 K/min.

3. Results and Discussion

We have investigated the influence of protein concentration on the structure and properties of biomineralized ZIF-90 crystals, using BSA as a model protein. We synthesized biocomposite samples by varying the concentration of BSA with fixed concentrations of zinc nitrate (100 mM) and 2-imidazolecarboxaldehyde (ICA, 25 mM). The final concentrations of BSA in ZIF-90 precursor solution ranged from 0 to 20 mg/mL. All reactions were conducted in water with a Zn/ICA molar ratio of 1:4. After mixing BSA and precursors, the solutions with different compositions were kept at room temperature (22–25 °C) for 4 h. The resultant particles were collected by centrifugation and washed with slightly alkaline water (pH > 7.2) three times.

It has been suggested that proteins serve as pre-nucleation sites and facilitate the nucleation and crystallization of ZIF crystals [10,19,39]. At low BSA concentration (0.1–0.5 mg/mL), the reaction solution turns turbid rapidly upon the addition and redispersion of BSA (Supplementary Video S1). The MOF crystals grow and precipitate within 40 min after the BSA addition. For BSA concentrations exceeding 1.2 mg/mL, the solution turned cloudy upon the addition of BSA and resulted in the formation of a much denser white precipitate. At the

highest BSA concentration studied here (20 mg/mL), the solution became cloudy initially, and with further mixing, it transitioned to a semi-transparent state (Supplementary Video S2). Without the addition of BSA, the rate of ZIF-90 formation is slower compared to when BSA is present, and the reaction solution did not turn turbid during the first 20 mins. The visual observation of the reaction solutions suggests that when BSA concentration is within 0.1–1 mg/mL, the rate of BSA-ZIF-90 crystal formation increases as the BSA concentration increases. At higher BSA concentrations, the excess BSA possibly disrupts the formation of well-defined BSA-ZIF-90 crystals.

To further probe the structural variations of BSA-embedded ZIF-90 crystals with varying BSA concentrations, we examined selected samples using high-angle annular dark-field scanning transmission electron microscopy (HAADF-HRSTEM), ESEM, XRD, and DSC. First, we investigated the particle size and morphology of different samples by BET, ESEM and HR-STEM (Figures 1 and 2). MOF crystals formed under various reaction conditions exhibited a tendency to adopt a rhombic dodecahedral structure (Figure 1), which corresponds to the stable structure of ZIF-90. With a BSA concentration of 0.1 mg/mL in the reaction solution, we found the average crystal size to be 1.0–1.5 μm from ESEM and HR-STEM images (Figures 1 and 2b). At this concentration, the BSA-ZIF-90 crystals exhibit a well-defined rhombic dodecahedral shape and are of similar size to pristine ZIF-90 crystals (Figure 1a), but the surface of BSA-ZIF-90 crystals was not as smooth as that of pristine ZIF-90 crystals. In the presence of BSA concentrations ranging from 0.5 to 1.2 mg/mL, the particles have an average size of 1.2–2.0 μm and maintain the rhombic dodecahedra structure but exhibit a rough and grainy surface (Figures 1c,d and 2c,d). The specific surface area and pore volume of the MOF crystals decreased upon loading the crystals with BSA. (Figure S1 and Table S1). The grainy surface and the presence of defects indicate that the encapsulation of higher concentrations of protein is beginning to disrupt the formation of the ZIF matrix, albeit not catastrophically. At BSA concentrations around 5 mg/mL, the estimated average size ranged from 2 to 5 μm, displaying a less well-defined rhombic dodecahedral morphology (Figures 1e and 2e). The pronounced granularity of particle surface and increased occurrence of defects in BSA-embedded ZIF-90 particles indicate reduced crystallinity at very high BSA concentrations. At a BSA concentration of 20 mg/mL, particle size decreased to approximately 500 nm, accompanied by an extremely rough surface (Figures 1f and 2f). At this concentration, the particles lack well-defined facets and appear to be surrounded by aggregated BSA-precursor complexes, suggesting that the excess biomolecules in the reaction solution hinder the growth of the nuclei into well-defined crystals.

Next, to further explore the effect of the concentration of encapsulated biomolecule on ZIF-90 crystals, we investigated the thermal properties and crystallinity of BSA-ZIF crystals using DSC and XRD. DSC revealed the progressive decay in the thermal stability of ZIF-based biocomposites with different BSA concentrations (Figure 3A,B). We observed that as the BSA concentration increased, the exothermic peak in the DSC curves of all seven samples consistently shifted to lower temperatures. Specifically, the exothermic peak shifted from 320 °C in pristine ZIF-90 to 270 °C in the ZIF-based biocomposites with a BSA concentration of 20 mg/mL. These shifts indicate a lower decomposition temperature during the pyrolysis process as the BSA content increases. High BSA loading within the ZIF-90 crystals partially disrupts the coordination between metal ions and organic linkers, lowering the thermal stability of the crystals.

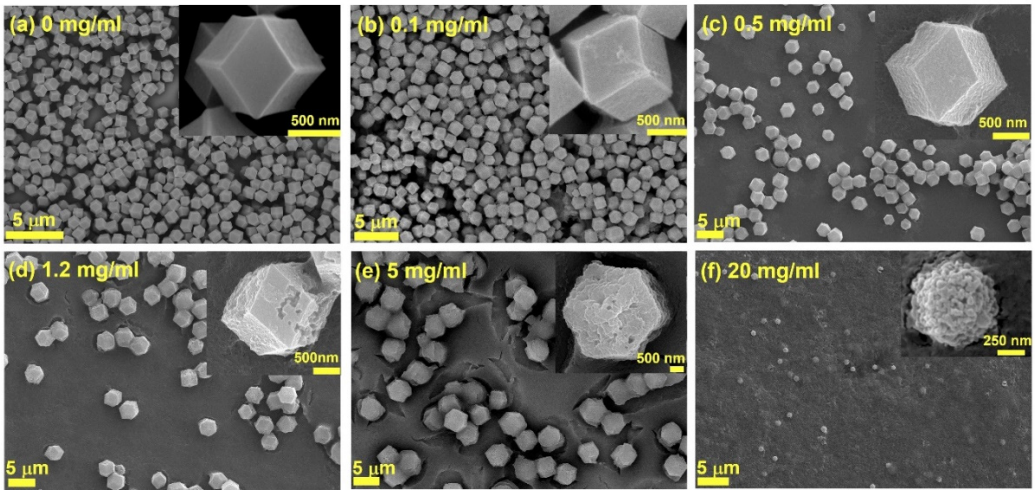

Figure 1. ESEM images of BSA-embedded ZIF-90 crystals with BSA concentrations of (**a**) 0 mg/mL, (**b**) 0.1 mg/mL, (**c**) 0.5 mg/mL, (**d**) 1.2 mg/mL, (**e**) 5 mg/mL, (**f**) 20 mg/mL.

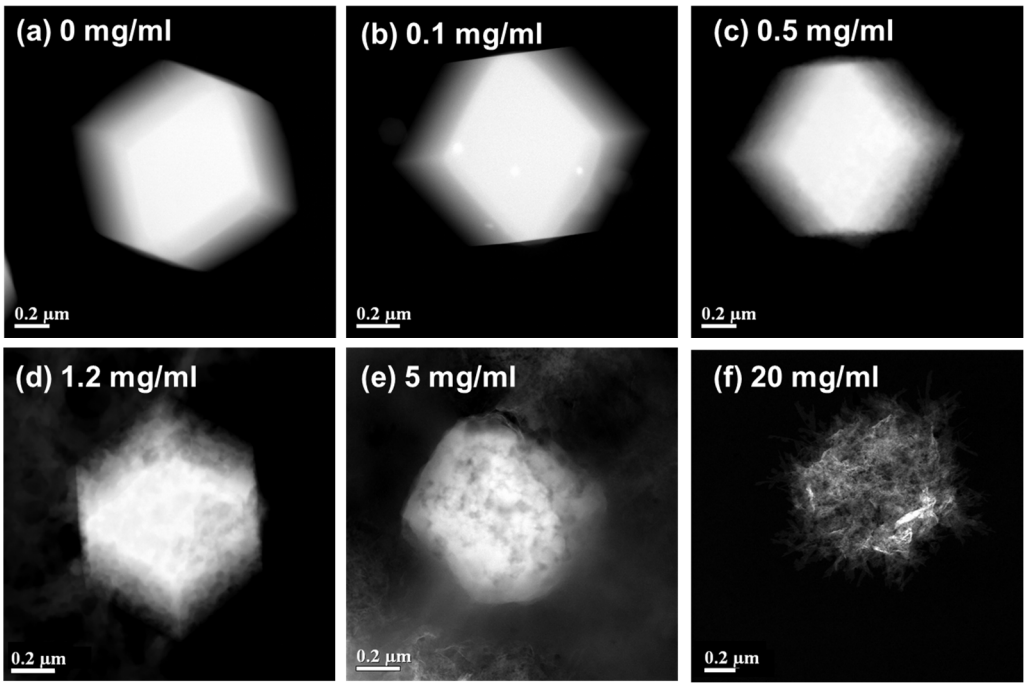

Figure 2. HAADF-HRSTEM images of BSA-embedded ZIF-90 crystals with BSA concentrations of (**a**) 0 mg/mL, (**b**) 0.1 mg/mL, (**c**) 0.5 mg/mL, (**d**) 1.2 mg/mL, (**e**) 5 mg/mL, (**f**) 20 mg/mL.

XRD is routinely employed to probe the crystal structure of pristine MOFs grown in solution and on surfaces. We determined the degree of crystallinity of pristine and protein-embedded ZIF-90 crystals by calculating the ratio of the areas of crystalline peaks to the total area of XRD peaks of each sample [41]. Crystallite size was determined by using the Bruker Topas software and Scherrer equation [41]. The predominant peaks of the pristine ZIF-90 sample (S0) at (110), (200), (211), (220), (310) and (222) are in good agreement with the literature, confirming the typical sodalite structure of ZIF-90 (Figure 3C), consistent with our ESEM and HR-STEM results (Figures 1A and 2A). From samples S0 to S6, which correspond to increasing BSA concentrations ranging from 0 mg/mL to 20 mg/mL, we observed a progressive broadening of the XRD peaks. This observation suggests a correlation between BSA concentration and crystallinity (Figure 3D). The crystallite size and crystallinity were found to decrease gradually with an increase in BSA concentrations encapsulated in ZIF-90 crystals (Figure 3D–F). The variations in particle size and morphology can be ascribed to the partial disruption in the crystalline framework in the presence of BSA. In the range of BSA concentrations from 0 to 1.2 mg/mL, the samples exhibit strong agreement with simulated ZIF-90 patterns, indicating that the incorporation of BSA did not significantly disrupt the long-range order and general morphology of the host MOF material. At BSA concentrations higher than 5 mg/mL, biocomposites show a significant decrease in crystallinity and an associated reduction in thermal stability (Figure 3B). This observation suggests that an increase in the amount of BSA embedded in the ZIF-90 crystals increases the defects in the crystals by disrupting the tight and extended metal-organic ligand coordination network observed in pristine crystals.

To explore the effect of increasing encapsulated biomolecule concentrations on the structure of biomolecules within BSA-ZIF-90 biocomposites, we obtained ATR-FTIR spectra of lyophilized biocomposite samples. This technique enables us to investigate the conformational changes of BSA embedded in the microcrystals [37,42–44]. Pristine ZIF-90 crystals exhibited absorption peaks at 1402–1467 cm^{-1} and 1680–1700 cm^{-1}, while pristine BSA exhibited absorption peaks at 1600–1700 cm^{-1}, 1500–1560 cm^{-1}, corresponding to amide I and amide II bonds of BSA [43], respectively (Figure 4A). FTIR spectra of BSA-ZIF-90 biocomposites shared the characteristic peaks of both ZIF-90 and BSA, suggesting the successful incorporation of BSA within ZIF-90 cystals [35,37,44,45]. Amide I involves the C=O stretching of CONH groups in proteins [37] and encompasses the major elements of proteins secondary structure, including α- helix, β-sheet/β-turn, random coils and extended chains [37,43,46,47]. Amide II primarily involves N-H bending and C-N stretching, which is less affected by the changes in the protein structure. Therefore, to decipher the interaction between BSA and ZIF-90 in the bicomposites, we analyzed the Amide I peak (1600–1700 cm^{-1}) with quantitative Voigt peak fitting to determine the secondary structure of BSA (Figure 4B–G). The FTIR vibrational frequency assignments are summarized in Table 1. To quantify the secondary structures, the percentage of each structure is calculated by measuring the area of the corresponding absorption band to the total area of all assigned bands in the FTIR spectrum. Among all the possible secondary structures of

lyophilized free BSA, α- helix is the dominant conformation with an estimated contribution of 46% (Figure 4H), which agrees with previous studies [42,43,46,48]. With an increase in the BSA concentration from 0.1 mg/mL to 2.5 mg/mL in the MOF crystals, there was a reduction in the contribution of MOF (1700–1680 cm^{-1}) (Figure 4C–F). Correspondingly, there was increased loss of α- helix (1655–1648 cm^{-1}), increase in β-turns (1684–1662 cm^{-1}), and extended chains (1620–1639 cm^{-1}), indicating that higher concentrations of encapsulated proteins lead to a higher possibility of unfolded protein structure. Additionally, there are increased contributions from short segment chains connecting α- helix segments and aggregated strands (1620–1630 cm^{-1}), alongside the presence of intermolecular β-sheet (1600–1616 cm^{-1}) at elevated BSA concentration. These changes indicate the partial denaturation/aggregation of BSA at high encapsulation concentrations during the formation of BSA-ZIF-90 microcrystals [46].

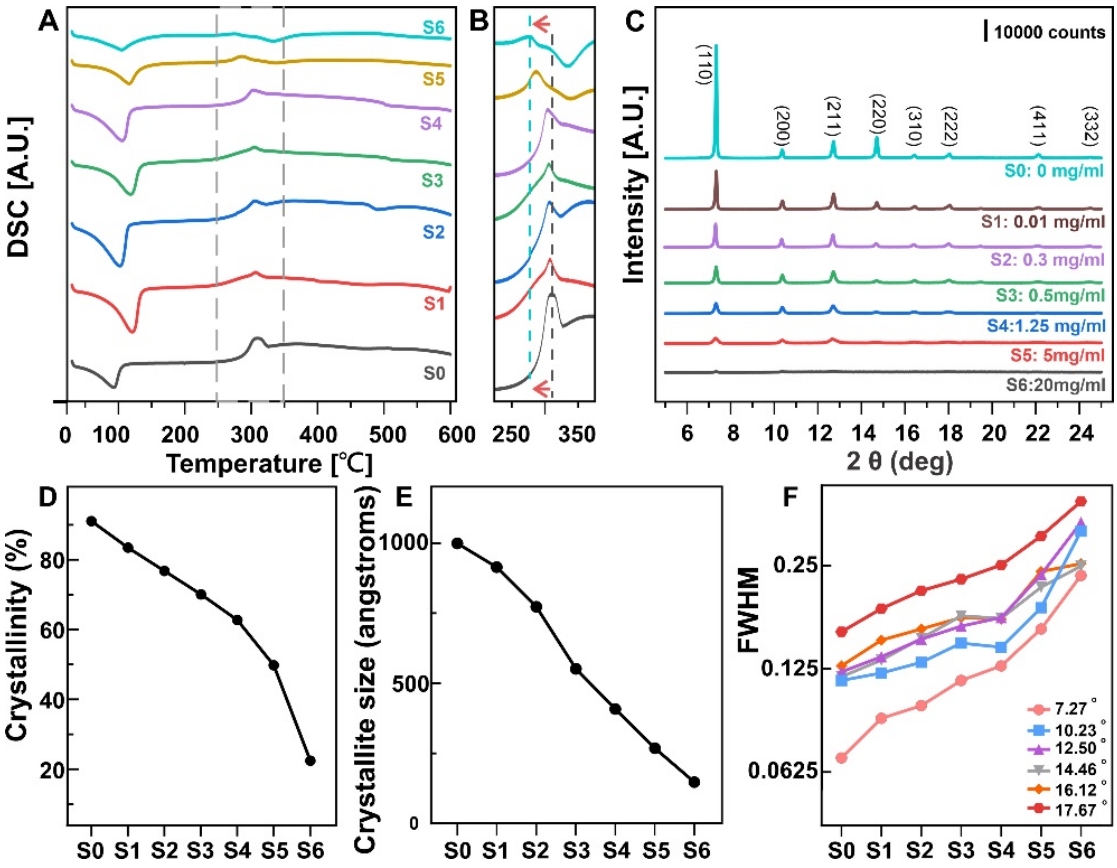

Figure 3. (**A**,**B**) DSC analysis of BSA-embedded ZIF-90 crystals with various BSA concentrations; (**C**) XRD analysis of BSA-embedded ZIF-90 crystals with various BSA concentrations; (**D**) Crystallinity; (**E**) and crystallite size analysis; (**F**) FWHM analysis.

Table 1. Vibrational frequency assignments of the MOF crystals and BSA.

Secondary Structure Assignment	Vibrational Frequency Range (cm^{-1})			
	Ref. [43]	Ref. [46]	Ref. [42]	This Work
MOF	-	-	-	1700–1680
β-Turns	1680–1663	1670–1662	1690–1660	1684–1662
α-Helix	1655–1650	1655–1650	1660–1650	1655–1648
Random coil	1646–1642	1645–1642	1648–1644	
Extended chains/ β-sheets/short-segment chains connecting the α-helical segment2	1639–1632	1638–1632	1640–1630	1639–1632
Extended chains/β-sheets, Aggregated strands	1630–1620		1630–1620	1630–1620
Side chain moieties/ Intermolecular β-sheet	1616–1600	1620–1610	1620–1600	1616–1600

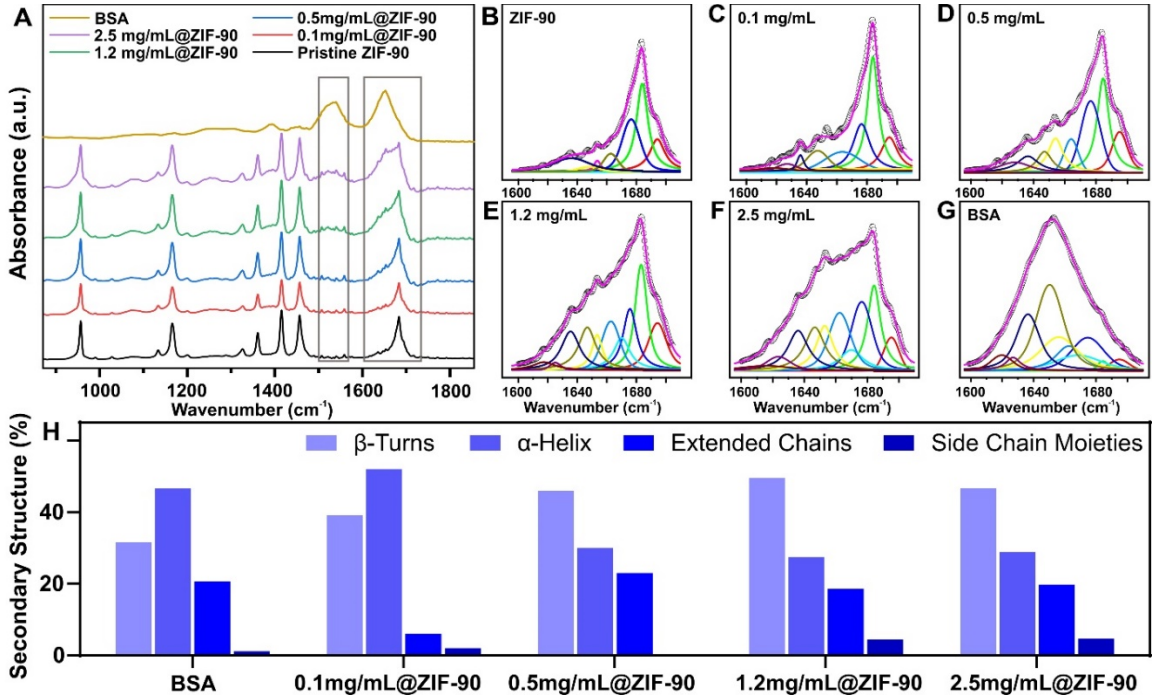

Figure 4. ATR-FTIR analysis of BSA-embedded ZIF-90 crystals with various BSA concentrations (**A**); deconvoluted ATR-FTIR spectra of the BSA-embedded ZIF-90 with BSA concentration of 0 mg/mL (**B**), 0.1 mg/mL (**C**), 0.5 mg/mL (**D**), 1.2 mg/mL (**E**), 2.5 mg/mL (**F**); Pristine BSA (**G**); Secondary structure analysis of BSA embedded in ZIF-90 crystals quantified by FTIR (**H**).

Lastly, we set out to evaluate the structure and biofunctionality of the biomolecules encapsulated in the biocomposites using HSA as a model protein. Samples were prepared by following the same protocol described above and analyzed using a commercial HSA enzyme-linked immunosorbent assay (ELISA) kit. The few BSA ELISA kits available commercially were not sufficiently sensitive. Hence, we have employed HSA as a model protein to investigate the loading density-dependent encapsulation and preservation. HSA and BSA have nearly 80% sequence homology, are similar structurally, and have similar binding pockets for various biomolecules [49] To increase the sensitivity and dynamic range of the assay, we converted this commercial colorimetric assay to a plasmonic fluor-linked immunosorbent assay (p-FLISA) [10]. The amount of HSA quantified by p-FLISA accounts for various possible losses of protein, including encapsulated and retrieved protein with compromised secondary structure, unencapsulated protein with lost secondary structure, and finite loss that may occur in the encapsulation and retrieval process. The preservation efficacy, defined here as the recognition by antibodies, was found to be above 85% with HSA concentrations in the range of 0.1–1 mg/mL for 1 week stored at 55 °C (Figure 5A) and above 80% with HSA concentrations in the range of 0.1–0.5 mg/mL for 2 weeks stored at 55 °C (Figure 5B). For HSA concentration above 1 mg/mL, the preservation efficacy was below 75% for 1-week storage and below 55% for 2-week storage at 55 °C (Figure 5). Statistical analysis demonstrates significant differences in preservation efficacy between MOF-encapsulated HSA in the concentration range of 0.1–1 mg/mL and the negative control (without MOF encapsulation) (Figure 5). Additionally, within the concentration range of 0.1–1 mg/mL, no significant differences were observed in preservation efficacy across these concentrations after storage for 2 weeks at 55 °C. The resultant optimal concentration range for achieving high preservation efficacy was in good agreement with the range of maintaining well-defined crystal structures. In the optimal concentration range of protein (0.1–1 mg/mL), biomolecules serve as pre-nucleation sites for the MOF precursors and promote the fast formation of ZIF-90 crystals with a well-defined rhombic dodecahedron shape (Figures 1b,c and 2b,c) and well-defined structure preserve the structure and biofuntionality of biomolecules (Figures 4 and 5). The small but finite loss of protein during the encapsulation and release significantly lowers the measured preservation efficacy of MOFs at extremely low protein concentrations (Figure 5). On the other hand, at high protein loading densities, the ZIF-90 structure becomes partially disrupted due to increased defects in the crystals (Figures 1e,f and 2e,f). Under these conditions, ZIF-90 fails to provide tight encapsulation of the proteins, leading to a loss of secondary structure and functionality, including antibody recognition (Figure 5). In addition, excess protein can be adsorbed on the surface of the crystals or remain unencapsulated in the solution. The denaturation of the unencapsulated proteins at high temperatures decreases preservation efficacy.

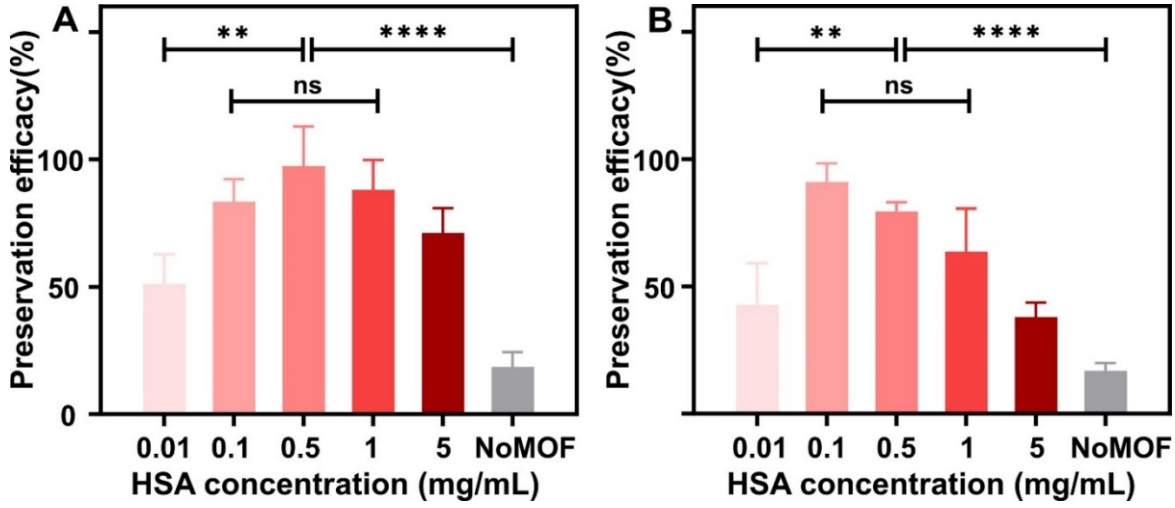

Figure 5. Preservation efficacy of HSA-embedded ZIF-90 particles stored at 55 °C for 1 week (**A**) and 2 weeks (**B**). (N = 3, ** $p < 0.01$, **** $p < 0.0001$, data represent mean ± s.d.).

4. Conclusions

We systematically investigated the effect of protein loading on the morphology and structure properties of ZIF-90 crystals by synthesizing ZIF-90-based biocomposites using albumin as a model protein. We demonstrated that the morphology, crystallinity, thermal stability, and preservation efficacy of the MOF are total protein concentration-dependent. The structure of albumin-encapsulated MOF crystals was stable when the total protein concentration was below 0.5 mg/mL. The protein structure and immunologic functionality of albumin were well-preserved when the encapsulated protein concentration was around 0.1–1 mg/mL. While the optimal concentration range for individual proteins might slightly vary, we believe the dependence of the MOF structure and properties on the protein loading density will be similar for various globular proteins. Our results will inform and facilitate future research in the burgeoning area of MOF biocomposites for biopreservation, drug delivery, and diagnostics.

Supplementary Materials: The following supporting information can be downloaded at: https://www.sciltp.com/journals/mi/2024/1/494/s1 , Figure S1: Nitrogen adsorption isotherms (A) and pore size distribution (B) of ZIF-90 and BSA-embedded ZIF-90 determined by Brunauer-Emmett-Teller (BET) and Barrett–Joyner–Halenda (BJH), respectively; Table S1: Specific surface area and pore dimensions of ZIF-90and BSA embedded -ZIF-90; Video S1: MOF encapsulation with low protein concentration; Video S2: MOF encapsulation with high protein concentration.

Author Contributions: S.S., S.T. and Y.W. designed the project. S.S. and Y.W. designed the experiments. Y.W. synthesized MOF and MOF based biocomposites. Y.W. performed protein encapsulation, recovery and bioassays. Y.W. performed SEM, TEM, DSC, BET and FTIR measurements. H.B. performed XRD measurements. J.J.M. helped to design the HSA related experiments. S.S., J.J.M. and Y.W. wrote the paper. All authors reviewed and commented on the manuscript. All authors have read and agreed to the published version of the manuscript.

Funding: This work was supported by the National Cancer Institute-Innovative Molecular Analysis Technologies (R21CA236652) and the National Science Foundation (CBET-2224610 and CBET-2316285).

Acknowledgments: The authors thank the Institute for Materials Science and Engineering (IMSE) at Washington University in St. Louis for providing access to characterization facilities. The authors also thank Young-Shin Jun for providing access to the FTIR spectrometer and Katherine M. Flores for providing access to the differential scanning calorimeter. The content is solely the responsibility of the authors and does not necessarily represent the official view of the National Institutes of Health (NIH) or the National Science Foundation (NSF).

Conflicts of Interest: The authors declare the following competing financial interest(s): S.S. and J.J.M. are inventors on a pending patent related to plasmonic-fluor technology, and the technology has been licensed by the Office of Technology Management at Washington University in St. Louis to Auragent Bioscience LLC. S.S. and J.J.M. are co-founders/shareholders of Auragent Bioscience LLC. S.S. and J.J.M., along with Washington University, may have financial gain through Auragent Bioscience, LLC through this licensing agreement.

References

1. Schrohl, A.S.; Würtz, S.; Kohn, E.; Banks, R.E.; Nielsen, H.J.; Sweep, F.C.; Brünner, N. Banking of biological fluids for studies of disease-associated protein biomarkers. *Mol. Cell. Proteom.* **2008**, *7*, 2061–2066. https://doi.org/10.1074/mcp.R800010-MCP200.
2. Chaigneau, C.; Cabioch, T.; Beaumont, K.; Betsou, F. Serum biobank certification and the establishment of quality controls for biological fluids: Examples of serum biomarker stability after temperature variation. *Clin. Chem. Lab. Med.* **2007**, *45*, 1390–1395. https://doi.org/10.1515/cclm.2007.160.

3. Luan, J.; Seth, A.; Gupta, R.; Wang, Z.; Rathi, P.; Cao, S.; Gholami Derami, H.; Tang, R.; Xu, B.; Achilefu, S.; et al. Ultrabright fluorescent nanoscale labels for the femtomolar detection of analytes with standard bioassays. *Nat. Biomed. Eng.* **2020**, *4*, 518–530. https://doi.org/10.1038/s41551-020-0547-4.
4. Livesey, J.H.; Ellis, M.J.; Evans, M.J. Pre-analytical requirements. *Clin. Biochem. Rev.* **2008**, *29*, S11–S15.
5. Evans, M.J.; Livesey, J.H.; Ellis, M.J.; Yandle, T.G. Effect of anticoagulants and storage temperatures on stability of plasma and serum hormones. *Clin. Biochem.* **2001**, *34*, 107–112. https://doi.org/10.1016/s0009-9120(01)00196-5.
6. Zhang, J.; Pritchard, E.; Hu, X.; Valentin, T.; Panilaitis, B.; Omenetto, F.G.; Kaplan, D.L. Stabilization of vaccines and antibiotics in silk and eliminating the cold chain. **2012**, *109*, 11981–11986, doi:doi:10.1073/pnas.1206210109.
7. Liang, K.; Ricco, R.; Doherty, C.M.; Styles, M.J.; Bell, S.; Kirby, N.; Mudie, S.; Haylock, D.; Hill, A.J.; Doonan, C.J. Biomimetic mineralization of metal-organic frameworks as protective coatings for biomacromolecules. *Nat. Commun.* **2015**, *6*, 1–8.
8. Wijesundara, Y.H.; Herbert, F.C.; Trashi, O.; Trashi, I.; Brohlin, O.R.; Kumari, S.; Howlett, T.; Benjamin, C.E.; Shahrivarkevishahi, A.; Diwakara, S.D.; et al. Carrier gas triggered controlled biolistic delivery of DNA and protein therapeutics from metal–organic frameworks. *Chem. Sci.* **2022**, *13*, 13803–13814. https://doi.org/10.1039/d2sc04982a.
9. Wang, C.; Sun, H.; Luan, J.; Jiang, Q.; Tadepalli, S.; Morrissey, J.J.; Kharasch, E.D.; Singamaneni, S. Metal–Organic Framework Encapsulation for Biospecimen Preservation. *Chem. Mater.* **2018**, *30*, 1291–1300. https://doi.org/10.1021/acs.chemmater.7b04713.
10. Wang, Y.; Morrissey, J.J.; Gupta, P.; Chauhan, P.; Pachynski, R.K.; Harris, P.K.; Chaudhuri, A.; Singamaneni, S. Preservation of Proteins in Human Plasma through Metal-Organic Framework Encapsulation. *ACS Appl. Mater. Interfaces* **2023**, *15*, 18598–18607. https://doi.org/10.1021/acsami.2c21192.
11. Liang, W.; Wied, P.; Carraro, F.; Sumby, C.J.; Nidetzky, B.; Tsung, C.K.; Falcaro, P.; Doonan, C.J. Metal-Organic Framework-Based Enzyme Biocomposites. *Chem. Rev.* **2021**, *121*, 1077–1129. https://doi.org/10.1021/acs.chemrev.0c01029.
12. Wang, A.; Walden, M.; Ettlinger, R.; Kiessling, F.; Gassensmith, J.J.; Lammers, T.; Wuttke, S.; Peña, Q. Biomedical Metal–Organic Framework Materials: Perspectives and Challenges. *Adv. Funct. Mater.* **2023**, *34*, 2308589. https://doi.org/10.1002/adfm.202308589.
13. Furukawa, H.; Cordova, K.E.; O'Keeffe, M.; Yaghi, O.M. The chemistry and applications of metal-organic frameworks. *Science* **2013**, *341*, 1230444.
14. Morris, W.; Doonan, C.J.; Furukawa, H.; Banerjee, R.; Yaghi, O.M. Crystals as Molecules: Postsynthesis Covalent Functionalization of Zeolitic Imidazolate Frameworks. *J. Am. Chem. Soc.* **2008**, *130*, 12626–12627. https://doi.org/10.1021/ja805222x.
15. Gao, S.; Hou, J.; Deng, Z.; Wang, T.; Beyer, S.; Buzanich, A.G.; Richardson, J.J.; Rawal, A.; Seidel, R.; Zulkifli, M.Y.; et al. Improving the Acidic Stability of Zeolitic Imidazolate Frameworks by Biofunctional Molecules. *Chem* **2019**, *5*, 1597–1608. https://doi.org/10.1016/j.chempr.2019.03.025.
16. Wang, C.; Sudlow, G.; Wang, Z.; Cao, S.; Jiang, Q.; Neiner, A.; Morrissey, J.J.; Kharasch, E.D.; Achilefu, S.; Singamaneni, S. Metal-Organic Framework Encapsulation Preserves the Bioactivity of Protein Therapeutics. *Adv. Healthc. Mater.* **2018**, *7*, e1800950. https://doi.org/10.1002/adhm.201800950.
17. Kang, L.; Smith, S.; Wang, C. Metal–Organic Framework Preserves the Biorecognition of Antibodies on Nanoscale Surfaces Validated by Single-Molecule Force Spectroscopy. *ACS Appl. Mater. Interfaces* **2020**, *12*, 3011–3020. https://doi.org/10.1021/acsami.9b19551.
18. Liang, K.; Coghlan, C.J.; Bell, S.G.; Doonan, C.; Falcaro, P. Enzyme encapsulation in zeolitic imidazolate frameworks: A comparison between controlled co-precipitation and biomimetic mineralisation. *Chem. Commun.* **2016**, *52*, 473–476.
19. Liang, W.; Xu, H.; Carraro, F.; Maddigan, N.K.; Li, Q.; Bell, S.G.; Huang, D.M.; Tarzia, A.; Solomon, M.B.; Amenitsch, H.; et al. Enhanced Activity of Enzymes Encapsulated in Hydrophilic Metal–Organic Frameworks. *J. Am. Chem. Soc.* **2019**, *141*, 2348–2355. https://doi.org/10.1021/jacs.8b10302.
20. Luzuriaga, M.A.; Herbert, F.C.; Brohlin, O.R.; Gadhvi, J.; Howlett, T.; Shahrivarkevishahi, A.; Wijesundara, Y.H.; Venkitapathi, S.; Veera, K.; Ehrman, R. Metal–Organic Framework Encapsulated Whole-Cell Vaccines Enhance Humoral Immunity against Bacterial Infection. *ACS Nano* **2021**, *15*, 17426–17438.
21. Luzuriaga, M.A.; Welch, R.P.; Dharmarwardana, M.; Benjamin, C.E.; Li, S.; Shahrivarkevishahi, A.; Popal, S.; Tuong, L.H.; Creswell, C.T.; Gassensmith, J.J. Enhanced stability and controlled delivery of MOF-encapsulated vaccines and their immunogenic response in vivo. *ACS Appl. Mater. Interfaces* **2019**, *11*, 9740–9746.
22. Ehrman, R.N.; Brohlin, O.R.; Wijesundara, Y.H.; Kumari, S.; Trashi, O.; Howlett, T.S.; Trashi, I.; Herbert, F.C.; Raja, A.; Koirala, S.; et al. A scalable synthesis of adjuvanting antigen depots based on metal–organic frameworks. *Chem. Sci.* **2024**, *15*, 2731–2744. https://doi.org/10.1039/d3sc06734c.
23. Liang, K.; Richardson, J.J.; Cui, J.; Caruso, F.; Doonan, C.J.; Falcaro, P. Metal–organic framework coatings as cytoprotective exoskeletons for living cells. *Adv. Mater.* **2016**, *28*, 7910–7914.

24. Wang, C.; Tadepalli, S.; Luan, J.; Liu, K.K.; Morrissey, J.J.; Kharasch, E.D.; Naik, R.R.; Singamaneni, S. Metal-Organic Framework as a Protective Coating for Biodiagnostic Chips. *Adv. Mater.* **2017**, *29*, 1604433. https://doi.org/10.1002/adma.201604433.
25. Velásquez-Hernández, M.d.J.; Linares-Moreau, M.; Astria, E.; Carraro, F.; Alyami, M.Z.; Khashab, N.M.; Sumby, C.J.; Doonan, C.J.; Falcaro, P. Towards applications of bioentities@MOFs in biomedicine. *Coord. Chem. Rev.* **2021**, *429*, 213651. https://doi.org/10.1016/j.ccr.2020.213651.
26. Zhang, H.; Lv, Y.; Tan, T.; van der Spoel, D. Atomistic Simulation of Protein Encapsulation in Metal-Organic Frameworks. *J. Phys. Chem. B* **2016**, *120*, 477–484. https://doi.org/10.1021/acs.jpcb.5b10437.
27. Wang, Y.; Wang, Z.; Gupta, P.; Morrissey, J.J.; Naik, R.R.; Singamaneni, S. Enhancing the Stability of COVID-19 Serological Assay through Metal-Organic Framework Encapsulation. *Adv. Healthc. Mater.* **2021**, *10*, e2100410. https://doi.org/10.1002/adhm.202100410.
28. Ogata, A.F.; Rakowski, A.M.; Carpenter, B.P.; Fishman, D.A.; Merham, J.G.; Hurst, P.J.; Patterson, J.P. Direct Observation of Amorphous Precursor Phases in the Nucleation of Protein-Metal-Organic Frameworks. *J. Am. Chem. Soc.* **2020**, *142*, 1433–1442. https://doi.org/10.1021/jacs.9b11371.
29. Carraro, F.; Williams, J.D.; Linares-Moreau, M.; Parise, C.; Liang, W.; Amenitsch, H.; Doonan, C.; Kappe, C.O.; Falcaro, P. Continuous-Flow Synthesis of ZIF-8 Biocomposites with Tunable Particle Size. *Angew. Chem. Int. Ed. Engl.* **2020**, *59*, 8123–8127. https://doi.org/10.1002/anie.202000678.
30. Troyano, J.; Carne-Sanchez, A.; Avci, C.; Imaz, I.; Maspoch, D. Colloidal metal-organic framework particles: The pioneering case of ZIF-8. *Chem. Soc. Rev.* **2019**, *48*, 5534–5546. https://doi.org/10.1039/c9cs00472f.
31. Carraro, F.; Velásquez-Hernández, M.d.J.; Astria, E.; Liang, W.; Twight, L.; Parise, C.; Ge, M.; Huang, Z.; Ricco, R.; Zou, X.; et al. Phase dependent encapsulation and release profile of ZIF-based biocomposites. *Chem. Sci.* **2020**, *11*, 3397–3404. https://doi.org/10.1039/C9SC05433B.
32. Linares-Moreau, M.; Brandner, L.A.; Velasquez-Hernandez, M.J.; Fonseca, J.; Benseghir, Y.; Chin, J.M.; Maspoch, D.; Doonan, C.; Falcaro, P. Fabrication of Oriented Polycrystalline MOF Superstructures. *Adv. Mater.* **2024**, *36*, e2309645. https://doi.org/10.1002/adma.202309645.
33. Lo, Y.; Lam, C.H.; Chang, C.-W.; Yang, A.-C.; Kang, D.-Y. Polymorphism/pseudopolymorphism of metal–organic frameworks composed of zinc(ii) and 2-methylimidazole: Synthesis, stability, and application in gas storage. *RSC Adv.* **2016**, *6*, 89148–89156. https://doi.org/10.1039/c6ra19437k.
34. Herbert, F.C.; Abeyrathna, S.S.; Abeyrathna, N.S.; Wijesundara, Y.H.; Brohlin, O.R.; Carraro, F.; Amenitsch, H.; Falcaro, P.; Luzuriaga, M.A.; Durand-Silva, A.; et al. Stabilization of supramolecular membrane protein-lipid bilayer assemblies through immobilization in a crystalline exoskeleton. *Nat. Commun.* **2021**, *12*, 2202. https://doi.org/10.1038/s41467-021-22285-y.
35. Tocco, D.; Chelazzi, D.; Mastrangelo, R.; Casini, A.; Salis, A.; Fratini, E.; Baglioni, P. Conformational changes and location of BSA upon immobilization on zeolitic imidazolate frameworks. *J. Colloid. Interface Sci.* **2023**, *641*, 685–694. https://doi.org/10.1016/j.jcis.2023.03.107.
36. Bakhshandeh, A.; Ardestani, F.; Ghorbani, H.R.; Darvish Ganji, M. Structural and molecular properties of complexes of biomolecules and metal-organic frameworks: Dispersion-corrected DFT treatment. *J. Mol. Model.* **2022**, *28*, 32. https://doi.org/10.1007/s00894-021-04947-2.
37. Mittal, A.; Gandhi, S.; Roy, I. Mechanistic interaction studies of synthesized ZIF-8 nanoparticles with bovine serum albumin using spectroscopic and molecular docking approaches. *Sci. Rep.* **2022**, *12*, 10331. https://doi.org/10.1038/s41598-022-14630-y.
38. Xu, Z.; Zhang, J.; Pan, T.; Li, H.; Huo, F.; Zheng, B.; Zhang, W. Encapsulation of Hydrophobic Guests within Metal–Organic Framework Capsules for Regulating Host–Guest Interaction. *Chem. Mater.* **2020**, *32*, 3553–3560. https://doi.org/10.1021/acs.chemmater.0c00684.
39. Marsh, C.; Shearer, G.C.; Knight, B.T.; Paul-Taylor, J.; Burrows, A.D. Supramolecular aspects of biomolecule interactions in metal–organic frameworks. *Coord. Chem. Rev.* **2021**, *439*, 213928. https://doi.org/10.1016/j.ccr.2021.213928.
40. Chen, G.; Huang, S.; Kou, X.; Zhu, F.; Ouyang, G. Embedding Functional Biomacromolecules within Peptide-Directed Metal-Organic Framework (MOF) Nanoarchitectures Enables Activity Enhancement. *Angew. Chem. Int. Ed. Engl.* **2020**, *59*, 13947–13954. https://doi.org/10.1002/anie.202005529.
41. Akhundzadeh Tezerjani, A.; Halladj, R.; Askari, S. Different view of solvent effect on the synthesis methods of zeolitic imidazolate framework-8 to tuning the crystal structure and properties. *RSC Adv.* **2021**, *11*, 19914–19923. https://doi.org/10.1039/d1ra02856a.
42. Schmidt, M.P.; Martinez, C.E. Kinetic and Conformational Insights of Protein Adsorption onto Montmorillonite Revealed Using in Situ ATR-FTIR/2D-COS. *Langmuir* **2016**, *32*, 7719–7729. https://doi.org/10.1021/acs.langmuir.6b00786.

43. Barreto, M.S.C.; Elzinga, E.J.; Alleoni, L.R.F. The molecular insights into protein adsorption on hematite surface disclosed by in-situ ATR-FTIR/2D-COS study. *Sci. Rep.* **2020**, *10*, 13441. https://doi.org/10.1038/s41598-020-70201-z.
44. Carpenter, B.P.; Talosig, A.R.; Mulvey, J.T.; Merham, J.G.; Esquivel, J.; Rose, B.; Ogata, A.F.; Fishman, D.A.; Patterson, J.P. Role of Molecular Modification and Protein Folding in the Nucleation and Growth of Protein-Metal-Organic Frameworks. *Chem. Mater.* **2022**, *34*, 8336–8344. https://doi.org/10.1021/acs.chemmater.2c01903.
45. Murty, R.; Bera, M.K.; Walton, I.M.; Whetzel, C.; Prausnitz, M.R.; Walton, K.S. Interrogating Encapsulated Protein Structure within Metal-Organic Frameworks at Elevated Temperature. *J. Am. Chem. Soc.* **2023**, *145*, 7323–7330. https://doi.org/10.1021/jacs.2c13525.
46. Lu, R.; Li, W.W.; Katzir, A.; Raichlin, Y.; Yu, H.Q.; Mizaikoff, B. Probing the secondary structure of bovine serum albumin during heat-induced denaturation using mid-infrared fiberoptic sensors. *Analyst* **2015**, *140*, 765–770. https://doi.org/10.1039/c4an01495b.
47. Ranjan, S.; Dasgupta, N.; Srivastava, P.; Ramalingam, C. A spectroscopic study on interaction between bovine serum albumin and titanium dioxide nanoparticle synthesized from microwave-assisted hybrid chemical approach. *J. Photochem. Photobiol. B* **2016**, *161*, 472–481. https://doi.org/10.1016/j.jphotobiol.2016.06.015.
48. Abrosimova, K.V.; Shulenina, O.V.; Paston, S.V. FTIR study of secondary structure of bovine serum albumin and ovalbumin. *J. Phys. Conf. Ser.* **2016**, *769*, 012016. https://doi.org/10.1088/1742-6596/769/1/012016.
49. Ketrat, S.; Japrung, D.; Pongprayoon, P. Exploring how structural and dynamic properties of bovine and canine serum albumins differ from human serum albumin. *J. Mol. Graph. Model.* **2020**, *98*, 107601. https://doi.org/10.1016/j.jmgm.2020.107601.